Journal of
Materials Chemistry C

Materials for optical, magnetic and electronic devices

Accepted Manuscript

This article can be cited before page numbers have been issued, to do this please use: J. García-Fernández, M. García-Carrión, A. Torres-Pardo, R. Martinez-Casado, J. Ramirez-Castellanos, E. Nogales, J. M. Gonzalez-Calbet and B. Mendez, *J. Mater. Chem. C*, 2020, DOI: 10.1039/C9TC05472C.

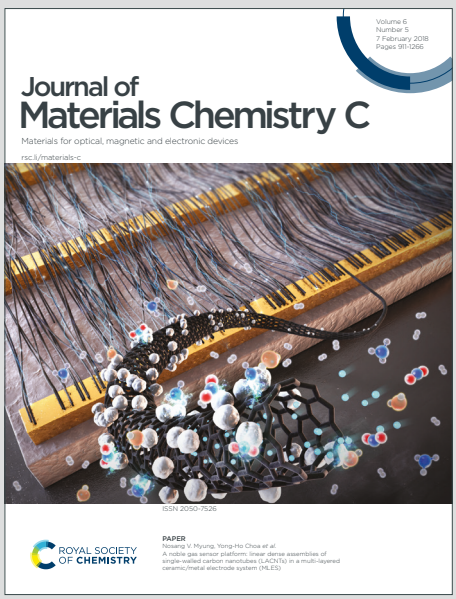

ROYAL SOCIETY OF CHEMISTRY

rsc.li/materials-c

View Article Online
DOI: 10.1039/C9TC05472C

Journal Name

ARTICLE TYPE

Cite this: DOI: 00.0000/xxxxxxxxxx

New insights into the luminescent properties of Na stabilized Ga-Ti oxides homologous series†

Javier García-Fernández,[a‡] Marina García-Carrión,[b‡] Almudena Torres-Pardo,[a] Ruth Martínez-Casado,[b] Julio Ramírez-Castellanos,[a] Emilio Nogales,[b] Jose González-Calbet [a,c] and Bianchi Méndez*[b]

Received Date
Accepted Date

DOI: 00.0000/xxxxxxxxxx

Herein, we achieve the synthesis and structural study of luminescent Na-stabilized Ga-Ti oxides homologous series by atomically resolved electron microscopy. Relevant optical properties as a function of the titanium content have been revealed. In particular, excitation and emission bands change with the series term, showing wide tunability of the luminescence bands, ranging from the ultraviolet to the infrared. First principles studies of these structures have been done in the framework of the density functional theory (DFT) to understand the optical properties. A good agreement with the experimental measurements for the three synthesized terms has been obtained from the compositional and occupancy of crystallographic sites perspective, as well as from the energy bands structure point of view. This work paves the way to explore further the capabilities of tuning electronic and optical properties into a variety of application fields.

1 Introduction

Wide band gap (WBG) semiconducting oxides, with bandgap energy (E_g) above 3.5 eV such as TiO_2, GeO_2, SnO_2 or Ga_2O_3, are attractive materials for a huge number of applications due to their multi-functionality[1,2]. Some applications for exploiting their interaction with ultraviolet radiation due to their large bandgap are UV-solar blind detectors, in photocatalytic processes or as transparent electrodes in photovoltaic devices[3–5]. Among the WBG oxides, Ga_2O_3 is recently attracting a lot attention due to not only their remarkable material properties but also to the availability of high quality substrates, which has provoked that most of the present research were focused on electronic devices[6], whereas less attention has been paid to their optical properties. Its wide band gap allows to be a suitable host for optical active impurities, such as Cr, Mn, Er, Eu, among others, leading to luminescence in the visible and near infrared electromagnetic spectrum range depending on the impurity of choice[7,8]. However, in order to exploit the full potential of WBG oxide materials in the optoelectronic devices arena, it would be quite desirable to engineer somehow their energy bandgap, which would dramatically affects their optical properties. Alloying semiconductors is an efficient route to provide tailored bandgap materials with modified optical/electrical properties[9]. In this way, several ternary Ga based compounds, such as $(Al_xGa_{1-x})_2O_3$ or $(In_xGa_{1-x})_2O_3$ have attempted to increase or decrease the bandgap, respectively[10,11]. Also, homologous series have recently attracted the interest for applications mainly focused on transparent electrodes, but also as luminescent materials for optoelectronic devices. Some examples in this field are $Ga_2O_3(ZnO)_m$ [12], $Ga_{3-x}In_3Ti_xO_{9+x/2}$ [13] or the Ga-Sn/Sb-Zn-O system[14]. In these phases, small variations in the cationic sublattice cause several changes in the electronic configuration and, as a consequence, in their properties relationships. Besides, another key actor when studying optical and electronic properties in semiconducting oxides is the presence of native structural defects, in particular oxygen vacancies, since they often provoke the appearance of electronic energy levels in the band gap and hence alter as well the electronic band structure.

One of the Ga based structural systems, the Na-Ga-Ti-O homologous series, has attracted particularly interest due to their good and tunable ionic conductivity, their photocatalytic activity or the feasible interaction of these structures with DNA molecules[15–17]. However, despite gallium oxide related materials could be the basis of some semiconducting devices, there is a lack of information about the luminescent and electronic properties of this system.

The introduction of Ti^{4+} ions into the β-gallia structure leads to the formation of different superstructures depending on the

[a] Department of Inorganic Chemistry, Faculty of Chemical Sciences, University Complutense of Madrid, E-28040 Madrid, Spain.
[b] Department of Materials Physics, Faculty of Physical Sciences, University Complutense of Madrid, E-28040 Madrid, Spain.
[c] ICTS National Center for Electron Microscopy, University Complutense Madrid, 28040, Madrid, Spain.
‡ These authors contributed equally to this work.
* E-mail: bianchi@ucm.es.

† Electronic Supplementary Information (ESI) available: HRTEM and DFT study of NGT1, NGT2 and NGT3 samples. See DOI: 00.0000/00000000.

View Article Online
DOI: 10.1039/C9TC05472C

atomic Ga:Ti ratio. When this ratio Ga:Ti ≥ 4, these phases can be described as ordered intergrowths of β-Ga_2O_3 units and TiO_2 octahedra, and as a result, hexagonal or orthogonal cross-shape tunnels are formed (Figure 1a and Figure 1b). However, if this ratio is lower than 4, a different structural type is obtained. In this case, the structure possesses both edge-sharing and corner sharing (Ga,Ti)O_6 octahedra, as well as corner sharing GaO_4 tetrahedra (Figure 1c). It is worth recalling that the phase stabilization can only be achieved via the incorporation of sodium cations into the biggest tunnels, causing the partial occupation of some Ti^{4+} by Ga^{3+} to keep the electroneutrality. As a consequence, the nominal formula results $Na_xGa_{4+x}Ti_{n-4-x}O_{2n-2}$ (n=5, 6 and 7 with x $\approx$ 0.7).

In this work, we describe the presence of UV-visible-IR emission bands in three different sodium gallium titanates (Na-Ga-Ti-O) corresponding to the terms n=5, 6 and 7, with x $\approx$ 0.7, of the $Na_xGa_{4+x}Ti_{n-4-x}O_{2n-2}$ homologous series, labeled as NGT1, NGT2 and NGT3, respectively, synthesized by the ceramic method. We show how the relationships between the structure and luminescent properties of n=5 and 6 are different of those observed for n=7. In this sense, a detailed study of the structure and properties of these materials is necessary in order to understand the luminescent behavior of these oxides and explore further technological applications of these materials.

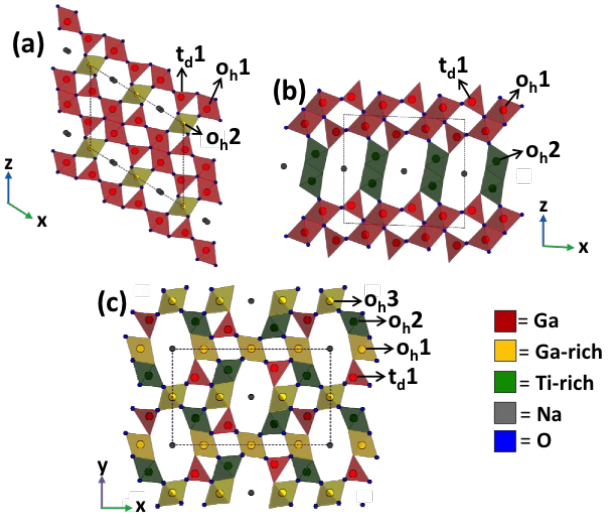

Fig. 1 Schematic structural model of (a) NGT1, (b) NGT2 and (c) NGT3. Color code: red, Ga occupation; yellow: Ga and Ti occupation being Ga in major ratio; green: Ga and Ti occupation being Ti in major ratio. Sodium and oxygen atoms are represented in grey and blue, respectively. Dashed lines indicate the unit cell.

2 Experimental methods

Synthesis procedure

Sodium gallium titanate $Na_xGa_{4+x}Ti_{n-4-x}O_{2n-2}$ (n = 5, 6 and 7; x $\approx$ 0.7) powders were prepared by solid-state reaction using the following starting materials: Na_2CO_3 (99.5% Sigma-Aldrich, Ga_2O_3 (99.99 % Sigma-Aldrich) and TiO_2 (99.9%, Sigma-Aldrich). The powders were pressed in pellets and heated up to 1225 °C inside an alumina crucible using sacrificial powders to avoid contamination and prevent sodium losses. Time reactions were 48 hours for the so-called NGT1 (n = 5) and NGT3 (n = 7) and 14 hours for NGT2 (n = 6), respectively. After that, the crucible was quenched in air.

Characterization techniques

X-ray diffraction (XRD) patterns were recorded using a Panalytical X'Pert Pro Alpha1 instrument, equipped with a primary fast X'Celerator detector operating at 45 kV and 40 mA, and fitted with a primary curved Ge (111) monochromator in order to obtain Cu $K_{\alpha 1}$ radiation ($\lambda = 1.5406$ Å). Data were collected at 2θ between 5° and 70°, with a step size of 0.008° and a collection time of 5 s/step.

Elemental quantification was performed by means of the inductively coupled plasma optical emission spectroscopy (ICP-OES) technique in an ARCOS equipment from SPECTRO by testing three specimens in liquid solution for each composition in order to minimize statistical errors. To prepare the solutions for the ICP-OES analysis, 0.050 mg of each sample was added to a 3 mL HNO_3, 1 mL HCl and 1 mL HF dissolution in a Teflon autoclave heated at 220 °C for 30 minutes using microwave radiation.

High-resolution transmission electron microscopy (HRTEM) was performed in a JEOL JEM 3000F electron microscope, fitted with a double-tilting goniometer stage (±22°, ±22°). Atomic resolution study was performed on a JEOL JEM ARM200 cF aberration-corrected scanning electron microscope (STEM) (Cold Emission Gun) operating at 120 kV (current emission density $\sim$ 1 pA and probe size $\sim$ 0.08 nm) to prevent sample damage. High angle annular dark field (HAADF) images were recorded using a nominal camera length of 60 mm and inner and outer collection semi-angles of 68 and 280 mrad, respectively. Annular bright field images were acquired at the same camera length, with collection semi-angles of 11 and 22 mrad. EELS experiments were acquired using a GIF-QuantumERTM with a collection semi-angle of 18 mrad and a convergence semi-angle of 20.3 mrad. EELS chemical maps were acquired with a pixel size $\sim$ 0.08 nm, over a total acquisition time of $\sim$ 2 min with an energy dispersion of 0.5 eV/channel. Principal Component Analysis with eight components was performed on EELS data set to denoise the spectra by using the MSA software package as a series of plug-in for Gatan DigitalMicrograph Suite[18]. For HRTEM and (S)TEM observations, the samples thus prepared were crushed in an agate mortar, then were ultrasonically dispersed in n-butanol and transferred to carbon coated copper grids. Structural models of the NGT oxides were created using CrystalMaker(CrystalMaker Software Ltd., Oxfordshire, U.K.).

On the other hand, cathodoluminescence (CL) studies were carried out in a Hitachi S2500 SEM. These spectra were acquired at room temperature, with the beam defocused and an acceleration voltage of V_{acc} = 20 kV. Photoluminescence (PL) and PL excitation (PLE) spectra were acquired with an Edinburgh Instruments FLS1000 system at room temperature, exciting with a 450 W Xe lamp as excitation source.

View Article Online
DOI: 10.1039/C9TC05472C

Density functional theory simulations

All DFT calculations have been performed using the CRYSTAL program,[19,20] in which the crystalline orbitals are expanded as a linear combination of atom-centered Gaussian orbitals, the basis set. The titanium, oxygen, gallium and sodium ions are described using all-electron basis sets contracted as s(8) p(6411) d(41), s(8) p(411) d(1), s(8) p(64111) d(41), s(8) p(511) d(1), respectively. Electronic exchange and correlation were approximated by using the HSE functional. In order to meet the required chemical composition, the supercells (1 x 3 x 1), (1 x 3 x 1), and (1 x 1 x 3) have been considered for NGT1, NGT2, NGT3, respectively. The internal coordinates have been determined by minimization of the total energy within an iterative procedure based on the total energy gradient calculated with respect to the nuclear coordinates. Table ESI-1 shows the atomic coordinates of the three investigated terms. Convergence was determined from the root-mean-square (rms) and the absolute value of the largest component of the forces. The thresholds for the maximum and the rms forces (the maximum and the rms atomic displacements) have been set to 0.00045 and 0.00030 (0.00180 and 0.0012) in atomic units. Geometry optimization was halted when all four conditions were satisfied simultaneously.

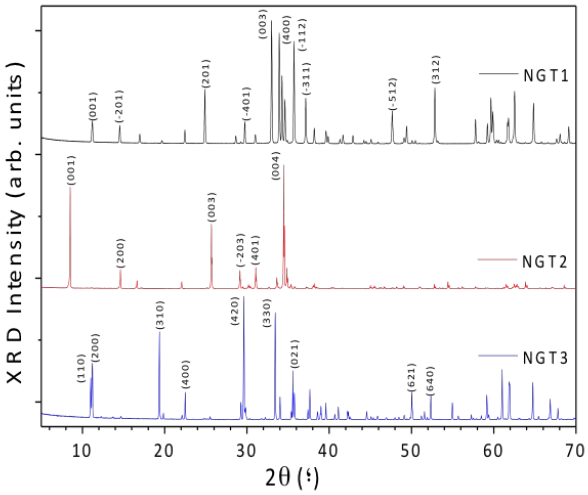

Fig. 2 XRD pattern of NGT1, NGT2 and NGT3 oxides. The most intense diffraction maxima have been indexed.

3 Results and discussion

Figure 2 shows the powder X-ray diffraction (XRD) patterns of all samples. The patterns for NGT1 and NGT2 materials can be indexed on the basis of a monoclinic C2/m unit cell (ICSD Collection code: 34196 and 59974), while NGT3 can be indexed according to an orthorhombic Pbam unit cell (ICSD Collection code: 74329). No impurities were detected. The unit cell parameters of each complex oxide and chemical composition determined by inductively coupled plasma optical emission spectroscopy (ICP-OES) analysis are depicted in Tables 1 and 2, respectively. The high crystallinity of the different phases has been studied by high resolution transmission electron microscopy (HRTEM) (see Supporting Information).

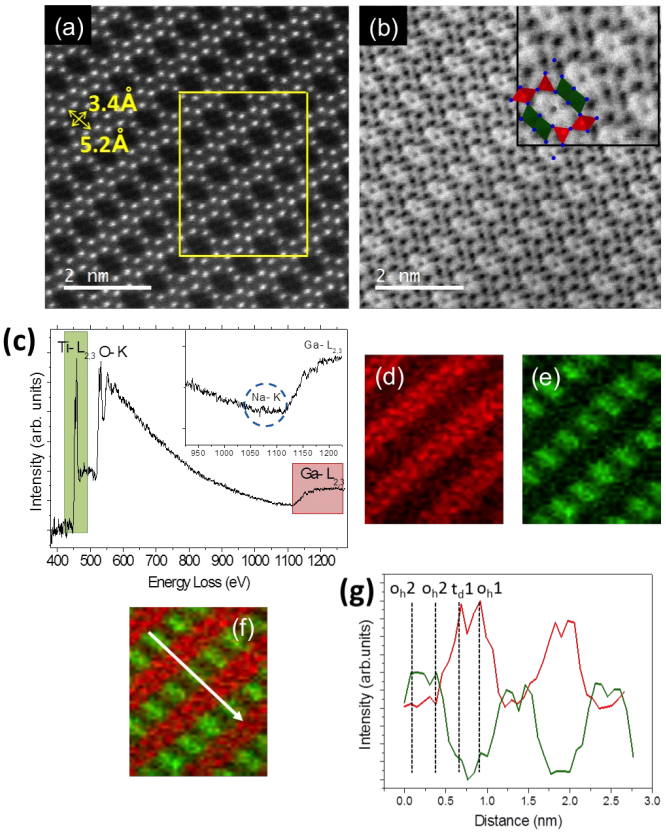

Fig. 3 (a) STEM HAADF image of NGT2 along [010] (the area marked with a yellow rectangle is used for the EELS study). (b) STEM ABF image along the same zone axis. The inset shows the positions of gallium (red), titanium (green), sodium (grey) and oxygen (blue) atoms. (c) EELS spectra sum acquired over the area marked in (a), showing the Ti-$L_{2,3}$, Ga-$L_{2,3}$, Na-K and O-K signals. Chemical maps obtained using EELS over the area marked in (a) are displayed in (d) Ga-$L_{2,3}$, (e) Ti-$L_{2,3}$ signals and (f) the sum of both. (g) Signal profiles of Ga (red) and Ti (green) elements obtained from EELS along the white marked arrow in (f).

Figure 3a shows the HAADF image[21] along the [010] zone axis of NGT2. Brighter atomic columns corresponding to Ga (Z= 31) and less bright columns corresponding to Ti (Z= 22) are observed arranged in an ordered intergrowth of β-gallia chains and two titanium columns. This arrangement leads to the formation of an orthogonal tunneled network with a diameter size of 5.2 × 3.4 Å. The simultaneously acquired ABF images[22] (Figure 3b) allow the visualization of lighter Na atomic columns positioned in the center of the tunnel. The inset of Figure 3b clearly shows the positions of the atomic oxygen columns defining the octahedral and tetrahedral coordination. In order to analyze the distribution of Ga and Ti, atomically resolved maps by electron energy loss spectroscopy (EELS) were acquired in the area marked with a yellow rectangle in the HAADF image. The sum spectrum obtained over the area of 11.30 nm^2 is depicted in Figure 3c. The chemical maps obtained from Ga-$L_{2,3}$ (red), Ti-$L_{2,3}$ (green) signals and the sum of both are displayed in Figure 3d-f. In order to evaluate the element distribution in the different polyhedra, the EELS intensity profile across the white arrow marked in Figure 3f is displayed

View Article Online
DOI: 10.1039/C9TC05472C

Table 1 Cell parameters for NGT1, NGT2 and NGT3 samples determined by XRD and DFT

Sample	a (Å)		b (Å)		c (Å)		β(°)	
	XRD	DFT	XRD	DFT	XRD	DFT	XRD	DFT
NGT1	12.361(7)	12.333(7)	3.002(1)	3.016(2)	9.366(3)	9.358(9)	122.09(1)	122.42
NGT2	12.103(5)	12.067(0)	3.009(2)	3.021(3)	10.409(4)	10.406(9)	92.25(1)	92.19
NGT3	15.815(5)	15.850(7)	9.332(2)	9.324(6)	2.997(2)	3.033(4)	90.00	90.00

Table 2 Experimental chemical composition obtained by ICP-OES for each sample

Sample	Elemental analysis			Experimental composition
	Na (% wt.)	Ga (% wt.)	Ti (% wt.)	
NGT1	3.9±0.3	64.8±1.5	3.1±0.3	$Na_{0.7\pm0.07}Ga_{4.7\pm0.1}Ti_{0.3\pm0.02}O_8$
NGT2	3.6±0.2	58.3±1.5	10.3±0.5	$Na_{0.8\pm0.05}Ga_{4.8\pm0.1}Ti_{1.2\pm0.05}O_{10}$
NGT3	2.9±0.2	49.6±1.5	17.4±1	$Na_{0.8\pm0.05}Ga_{4.8\pm0.1}Ti_{2.2\pm0.1}O_{12}$

in Figure 3g. Ga is located in t_d1 and o_h1, while Ti and Ga signals are detected in o_h2 positions (see Figure 1b). This elemental mapping unambiguously confirms the proposed structure by Y. Michue *et al.*[23] for NGT2 member of the series.

A similar analysis was carried out on NGT3 sample. Figures 4a and 4b show the HAADF and ABF images along [001]. From these images, atomic resolution structure (including Na atomic columns) as well as tunnel size (5.8 × 3.2 Å) is clearly visualized. Over an area of 8.83 nm^2 marked in yellow in 4a, we have obtained the sum spectra depicted in Figure 4c confirming the identification of Na, Ga, Ti, and O in the sample. Figures 4d-f show the obtained chemical maps for Ga-$L_{2,3}$ (red), Ti-$L_{2,3}$ (green) and the sum of Ga and Ti, respectively. From the mapping results, it is clearly observed that every orthogonal tunnel is majority formed by two titanium-rich atomic columns and six gallium-rich atomic columns (marked in Figure 4f). Effectively, the intensity profile (Figure 4g) from Ga-$L_{2,3}$ (red), Ti-$L_{2,3}$ (green) signals running along the white arrow (Figure 4f) clearly reveals the alternation of one t_d1 fully occupied by Ga and two octahedra, o_h1 Ga-rich and o_h2 Ti-rich, (see Figure 1c), in good agreement with the structure proposed by Y. Michue et al.[24] Notice that in this analysis o_h3 Ga-rich are not included due to the very low concentration of Ti (around 8 %) at those positions.

With the aim to study the bandgap and electronic states of these compounds, which affect the recombination processes and carrier dynamics that are relevant for applications, light emission and excitation properties have been analyzed by several luminescence techniques. Figure 5 shows cathodoluminescence (CL) excited with the electron beam of a scanning electron microscope (SEM), photoluminescence (PL) excited with a monochromated light beam from a Xe lamp and PL excitation (PLE) spectra corresponding to the three synthesized terms. Spectra obtained from each sample under electron beam and light excitation are shown in the same graph, so that they can be readily compared. Figure 5a shows the luminescence spectra corresponding to NGT1. CL spectrum (red line) is dominated by a broad band centered at 2.4 eV (500 nm). Besides, two less intense bands are observed in the ultraviolet (UV) range, at 3.7 and 4.8 eV. On the other hand, PL emission (black line) only shows the broad visible band, but now centered at around 2.3 eV (540 nm) and a width slightly lower than that of the CL spectrum. Therefore, a slight shift is observed for the PL maximum with respect to that of CL. The differences in position and relative intensity of the emission bands observed by CL and PL of the same sample occur often and are usually related to the severe differences in energy and excitation density between the CL and PL techniques.

The presence of UV-visible-IR emission bands in gallium oxide and titanium oxide is usually related to the presence of point defects, such as oxygen vacancies, cation vacancies or vacancy pairs[25]. Therefore, in the case of these Ga-Ti compounds, it is expected that the origin of the observed bands, could be mainly due to this type of defects. The fact that they are broad and possibly composed of several emission bands is consistent with the bands associated to this kind of defects in other oxides. For example, complex defect-related emission in the visible region has been reported in zinc germanates (Zn_2GeO_4)[26]. However, no previous work could be found with an analysis about the luminescence of the compounds studied in this work, being the present results the first ones to our knowledge. Here, we would draw the first conclusions about the origin of these bands in alkali doped beta-gallia-rutile crystals, and hence, further and more detailed work will be needed in order to assess the origin of these bands.

Figure 5b shows CL and PL spectra for NGT2. It is again observed that the dominant emission band in the CL spectrum is centered at 2.5 eV (500 nm), but it is appreciably wider than that found in NGT1 sample. This result indicates that the structure of luminescent defects related to this band is more complex in the second term than in the first one. Similar to NGT1, there are weak bands in the UV region, one of them appearing as a shoulder of the visible band, while the other one, centered around 4.5 eV, is resolved. On the other hand, PL emission presents a band centered in 2.2 eV, similar to that found in NGT1, but slightly narrower. As in the case of sample NGT1, PL band is slightly shifted to lower energies with respect to the CL one. Finally, Figure 5c shows spectra from term NGT3, with a wide CL emission band centered in the visible, around 2.8 eV (450 nm), i.e. an energy that is slightly higher than that of the most intense bands of the other two terms. However, the most relevant difference in comparison to the luminescence spectra obtained from the other terms is that this visible band is not the dominant one, but a band in the near-IR range, centered in 1.6 eV (775 nm). This near-IR band is also observed in the PL spectrum with the same characteristics as the CL one. It is noteworthy that crystal structure from this term NGT3 is different from that of the other two terms, as

View Article Online
DOI: 10.1039/C9TC05472C

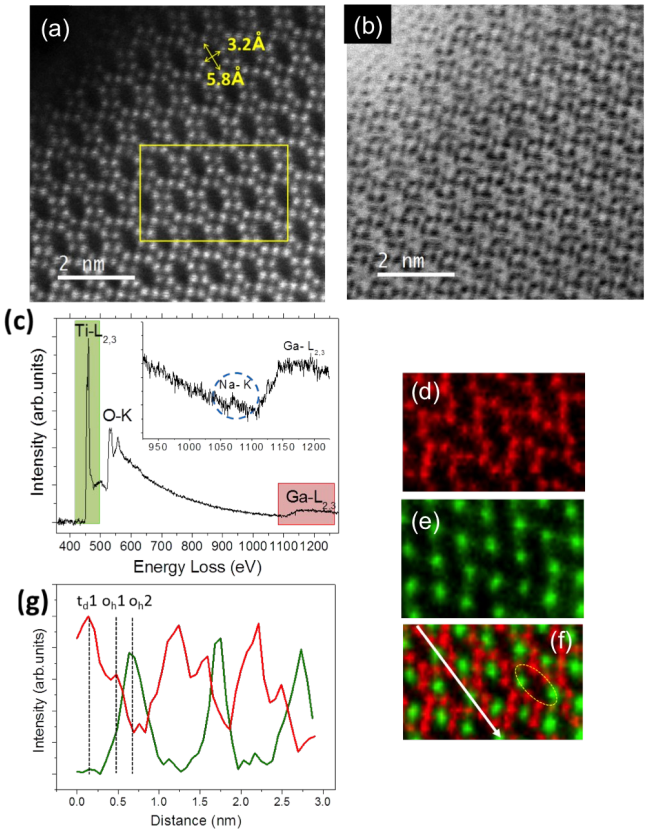

Fig. 4 (a) STEM HAADF image of NGT3 along [001] (the area marked with a yellow rectangle is used for the EELS study). (b) STEM ABF image along the same zone axis. (c) EELS spectra sum acquired over the area marked in (a), showing the Ti-$L_{2,3}$, Ga-$L_{2,3}$, Na-K and O-K signals. The inset shows an enhancement of the EELS spectra confirming the detection of Na-K signal. Chemical maps obtained using EELS over the area marked in (a) are displayed in (d) Ga-$L_{2,3}$, (e) Ti-$L_{2,3}$ signals and (f) the sum of both. (g) Signal profiles of Ga (red) and Ti (green) elements obtained from EELS along the white marked arrow in (f).

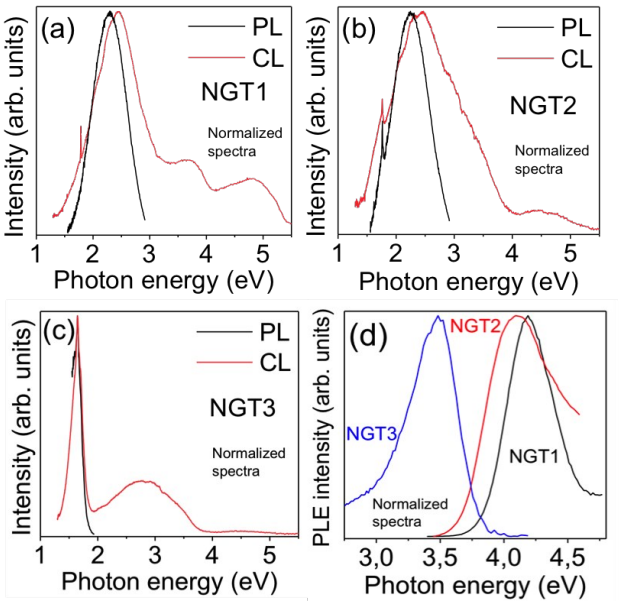

Fig. 5 CL (red line) and PL (black line) spectra from (a) NGT1, (b) NGT2 and (c) NGT3 terms. (d) PLE spectra from the three terms. Excitation wavelengths for the PL spectra were 295 nm (4.2 eV), 302 nm (4.1 eV) and 360 nm (3.4 eV) for terms NGT1, NGT2 and NGT3, respectively, while emission wavelengths for PLE spectra in (d) were 530 nm (2.3 eV), 550 nm (2.2 eV), 750 nm (1.6 eV), respectively.

previously discussed. This fact is likely to be related to the larger difference between luminescence of term NGT3 with respect to terms NGT1 and NGT2. In fact, as mentioned above, luminescence bands in this kind of oxides are usually related to point defects, influenced by the local symmetry of the center. Figure 5 shows that the local surrounding for both the cations and oxygens in terms NGT1 and NGT2 is reasonably similar, but there is a noticeable change for term NGT3, where both edge-sharing and corner sharing octahedra are present with different fractional occupancy values, e.g. appearing the o_h3 site, not present in the first two terms. This can be related to the greater difference in the luminescence behavior of term NGT3.

Figure 5d shows PLE spectra corresponding to the three terms of the series. The spectra have been obtained from each term by monitoring the wavelength corresponding to the maximum PL intensity, i.e. the wavelength where the dominant luminescence band is centered: λ_{em1} =530 nm (2.3 eV) for NGT1, λ_{em2} =550 nm (2.2 eV) for NGT2 and λ_{em3} =750 nm (1.6 eV) for NGT3. It is shown that excitation bands maxima shift to lower energies as term number, n, increases, i.e. as Ti content increases. From these PLE spectra, the band gap value, E_g, is obtained[27] for each term: E_{g1} = 4.2 eV, E_{g2} = 4.1 eV, E_{g3} = 3.5 eV. These values are in fair agreement with those reported previously, obtained by diffuse reflectance: E_{g1rep} = 4.15 eV, E_{g2rep} = 3.72 eV, E_{g3rep} = 3.42 eV[17]. Indeed, the values obtained for terms 1 and 3 are in very good agreement, with a difference of 1-2 %. On the other hand, the value obtained for term 2 differ by about a 10 %, being higher the value obtained by PLE.

The theoretical analysis of the three terms has been assisted by the use of ab initio calculations of the structure. The sodium gallium titanate, as other oxides, represents a challenge for standard implementations of Density Functional Theory (DFT). Generalized gradient approximations (GGA) functionals often underestimate the band gap, but the use of hybrid exchange functionals provides a qualitatively correct description of the structure, energetics and electronic properties for many different materials, and in particular, for oxides[28]. The method adopted here is DFT using the screened hybrid exchange functional HSE. The HSE functional has the advantage that partially corrects for electronic self-interaction and so yields qualitatively correct fundamental band gaps in wide band gap semiconductors[28,29].

The distinctive feature of disordered systems such as the sodium gallium titanate, is the lack of order in the occupancy of a given set of crystallographic sites by a set of species. This kind of structure is often described by introducing the concept of fractional occupancy, which cannot be easily adopted in computational modeling. In order to simulate the compound it is necessary to consider all the crystallographic sites involved in the fractional occupancy, whose number essentially depends on the size of the periodic cell taken as a reference. Symmetry analysis

View Article Online
DOI: 10.1039/C9TC05472C

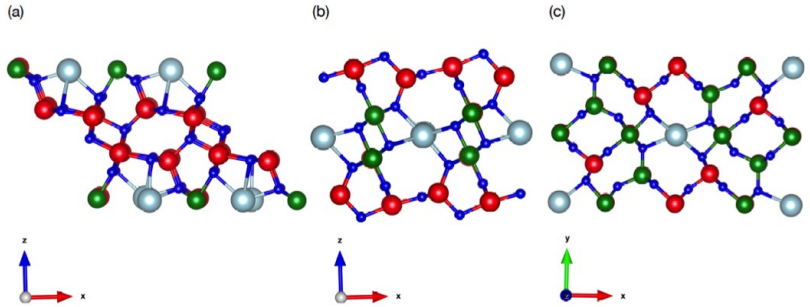

Fig. 6 DFT optimized structures for (a) NGT1, (b) NGT2, and (c) NGT3. The red, green, grey, and blue balls correspond to Ga, Ti, Na, and O, respectively.

permits to recognize equivalences between configurations, and therefore in order to fully characterize the system, it is sufficient to compute one representative configuration of the symmetry independent ones. The more stable configurations for the three terms can be seen in Figure 6. It has to be noticed that all of them are in perfect agreement with the ones presented in [17] . Both the lattice parameters (see Table 1) and band gaps for each term (E_{g1} = 4.7 eV, E_{g2} = 4.6 eV, E_{g3} = 3.8 eV) are in very good agreement with the corresponding experimental ones presented here. The energy differences between terms is preserved, being the values systematically around 10 % larger than the experimental ones, as usually happens with DFT calculations [30]. In summary, electronic and crystal structure of the three terms of sodium gallium titanate has been characterized from an experimental and theoretical point of view for the first time. DFT calculations confirm the band gap and cell parameters obtained experimentally.

4 Conclusions

Three terms of the $Na_xGa_{4+x}Ti_{n-4-x}O_{2n-2}$ homologous series (n= 5, 6 and 7 with x ≈ 0.7) have been synthesized as single phases. Their structures have been studied by atomic resolution electron microscopy and DFT for the first time. In addition, light emission and excitation properties are analyzed, revealing the presence of different broad UV-visible-IR emission bands as a function of the composition. Particularly, luminescence can be tuned in a very wide range, moving from UV and visible bands for the n = 5 and 6 terms, i.e., those with lower Ti content, to a dominant infrared emission band for the n = 7 member. The effect of Ti content on the band gap values was also investigated, being all of them higher than 3.5 eV. The theoretical DFT calculations confirm the band gap as well as the exact occupancy, crystallographic sites, and cell parameters experimentally observed. These results can widen the performance and applicability of these materials in the field of tunable optoelectronic devices.

Conflicts of interest

There are no conflicts to declare.

Acknowledgements

This work was supported by the Spanish Ministry of Innovation, Science and Technology and Spanish Ministry of Economy through Research Projects MAT2014-54372-R, MAT-2015-65274-R/FEDER, MAT2016-81720-REDC, MAT2017-82252-R, RTI2018-097195-B-I00 and M-ERA.NET PCIN-2017-106. We thank the National Center of Electron Microscopy (UCM) for facilities.

Notes and references

1 J. G. Lu, P. Chang and Z. Fan, *Materials Science and Engineering: R: Reports*, 2006, **52**, 49 – 91.
2 S. J. Pearton, J. Yang, P. H. Cary, F. Ren, J. Kim, M. J. Tadjer and M. A. Mastro, *Applied Physics Reviews*, 2018, **5**, 011301.
3 L. Li, P. S. Lee, C. Yan, T. Zhai, X. Fang, M. Liao, Y. Koide, Y. Bando and D. Golberg, *Advanced Materials*, 2010, **22**, 5145–5149.
4 C. Sotelo-Vazquez, R. Quesada-Cabrera, M. Ling, D. O. Scanlon, A. Kafizas, P. K. Thakur, T.-L. Lee, A. Taylor, G. W. Watson, R. G. Palgrave, J. R. Durrant, C. S. Blackman and I. P. Parkin, *Advanced Functional Materials*, 2017, **27**, 1605413.
5 T. Minami, *Semiconductor Science and Technology*, 2005, **20**, S35–S44.
6 M. Higashiwaki, K. Sasaki, A. Kuramata, T. Masui and S. Yamakoshi, *Applied Physics Letters*, 2012, **100**, 013504.
7 E. Nogales, B. Méndez, J. Piqueras and J. A. García, *Nanotechnology*, 2009, **20**, 115201.
8 I. López, E. Nogales, B. Méndez, J. Piqueras, A. Peche, J. Ramírez-Castellanos and J. M. González-Calbet, *The Journal of Physical Chemistry C*, 2013, **117**, 3036–3045.
9 Y. Zhu, X. Lang and Q. Jiang, *Advanced Functional Materials*, 2008, **18**, 1422 – 1429.
10 T. Oshima, T. Okuno, N. Arai, Y. Kobayashi and S. Fujita, *Japanese Journal of Applied Physics*, 2009, **48**, 070202.
11 I. López, A. D. Utrilla, E. Nogales, B. Méndez, J. Piqueras, A. Peche, J. Ramírez-Castellanos and J. M. González-Calbet, *The Journal of Physical Chemistry C*, 2012, **116**, 3935–3943.
12 Y. Michiue, T. Mori, A. Prytuliak, Y. Matsushita, M. Tanaka and N. Kimizuka, *RSC Adv.*, 2011, **1**, 1788–1793.
13 K. Rickert, P. Boullay, S. Malo, V. Caignaert and K. Poeppelmeier, *Inorganic Chemistry*, 2016, **55**, 4403–4409.
14 S. Eichhorn, H. Schmid, W. Assenmacher and W. Mader, *Journal of Solid State Chemistry*, 2017, **246**, 214 – 220.
15 D. Edwards, N. H. Empie, N. Meethong and J. W. Amoroso, *Solid State Ionics*, 2006, **177**, 1897 – 1900.
16 N. Empie and D. Edwards, *Langmuir : the ACS journal of surfaces and colloids*, 2006, **22**, 7658–63.

View Article Online
DOI: 10.1039/C9TC05472C

17 S. Sanford, S. T. Misture and D. D. Edwards, *Journal of Solid State Chemistry*, 2013, **200**, 189 – 196.

18 M. Bosman, M. Watanabe, D. Alexander and V. Keast, *Ultramicroscopy*, 2006, **106**, 1024 – 1032.

19 R. Martinez-Casado, V. H.-Y. Chen, G. Mallia and N. Harrison, *The Journal of Chemical Physics*, 2016, **144**, 184702.

20 R. Dovesi, A. Erba, R. Orlando, C. M. Zicovich-Wilson, B. Civalleri, L. Maschio, M. Rrat, S. Casassa, J. Baima, S. Salustro and B. Kirtman, *Wiley Interdisciplinary Reviews: Computational Molecular Science*, 2018, **8**, e1360.

21 S. Pennycook and D. Jesson, *Ultramicroscopy*, 1991, **37**, 14 – 38.

22 E. Okunishi, H. Sawada and Y. Kondo, *Micron*, 2012, **43**, 538 – 544.

23 Y. Michiue and A. Sato, *Acta Crystallographica Section B*, 2004, **60**, 692–697.

24 Y. Michiue, T. Sasaki, M. Watanabe and Y. Fujiki, *Materials Research Bulletin*, 1993, **28**, 173 – 178.

25 K. Shimamura, E. G. Villora, T. Ujiie and K. Aoki, *Applied Physics Letters*, 2008, **92**, 201914.

26 P. Hidalgo, A. Lopez, B. Mendez and J. Piqueras, *Acta Materialia*, 2016, **104**, 84–90.

27 H. Masai, Y. Yamada, Y. Suzuki, K. Teramura, Y. Kanemitsu and T. Yoko, *Scientific reports*, 2013, **3**, 3541.

28 A. V Krukau, O. A Vydrov, A. F Izmaylov and G. E Scuseria, *The Journal of chemical physics*, 2007, **125**, 224106.

29 B. G. Janesko, T. M. Henderson and G. E. Scuseria, *Phys. Chem. Chem. Phys.*, 2009, **11**, 443–454.

30 P. Pernot, B. Civalleri, D. Presti and A. Savin, *The Journal of Physical Chemistry A*, 2015, **119**, 5288 – 5304.

View Article Online
DOI: 10.1039/C9TC05472C